INTERNATIONAL JOURNAL FOR NUMERICAL METHODS IN FLUIDS
Int. J. Numer. Meth. Fluids 0000; **00**:1–29 *Prepared using* fldauth.cls *[Version: 2002/09/18 v1.01]*

An Adaptive Finite Element Method for Inviscid Compressible Flow

Murtazo Nazarov*† and Johan Hoffman

Computational Technology Laboratory,
School of Computer Science and Communication,
Royal Institute of Technology KTH,
SE-10044 Stockholm, Sweden.

SUMMARY

We present an adaptive finite element method for the compressible Euler equations, based on a posteriori error estimation of a quantity of interest in terms of a dual problem for the linearized equations. Continuous piecewise linear approximation is used in space and time, with componentwise weighted least squares stabilization of convection terms, and residual based shock-capturing. The adaptive algorithm is demonstrated numerically for the quantity of interest being the drag force on a body. Copyright © 0000 John Wiley & Sons, Ltd.

KEY WORDS: adaptive finite element method, a posteriori error estimation, dual problem, compressible Euler equations, circular cylinder, wedge

1. Introduction

In this paper we present an adaptive finite element method for 3D time dependent compressible fluid flow. The Euler equations express conservation of mass, momentum and energy, and describe the motion of a Newtonian fluid, in the limit of vanishing viscosity in the Navier-Stokes equations. Past an object, flow with vanishing viscosity develop turbulence, shock waves, rarefactions and discontinuities. These phenomena need to be well resolved by the finite element method in order to get high accuracy in computations. Uniform refinement of the finite element mesh is not an option due to the high cost, so instead efficient algorithms for local adaptation of the mesh are needed. An *ad hoc* way of identifying regions for local mesh adaptation can be to use the size of the gradient of the solution or the residual of the system as an error indicator, with other possible error indicators in [1, 2].

The adaptive algorithm in this paper is based on *a posteriori* error estimation, where the error is estimated from a computed solution. In most applications we are interested in

*Correspondence to: Murtazo Nazarov, School of Computer Science and Communication, Royal Institute of Technology KTH, Lindstedtsvägen 3, SE-10044 Stockholm, Sweden.
†E-mail: murtazo@csc.kth.se

Received 31 August 2009
Revised 26 February 2010
Accepted 2 March 2010

controlling the error in some *quantity of interest* or *output*, rather than the error itself. The quantity of interest can be fluid forces such as drag and lift, stresses or fluxes. Once an a posteriori bound of the error in an output of interest is available, it is possible to improve the approximation in order to reduce this error, which makes the method efficient and reliable. We base our work on the general framework for a posteriori error estimation developed by Erikson and Johnson, Becker and Rannacher, with co-workers, [3, 4, 5, 6, 7].

For systems of conservation laws, a posteriori error analysis was developed in [8, 9, 10], adaptive discontinuous Galerkin methods for stationary compressible Euler equations in 2D were developed in [11, 12, 13, 14], and in [15] a posteriori error estimation for the time-dependent compressible Euler equations was analysed with numerical simulations in 2D.

In this paper we present a posteriori error estimates for the general problems of the time-dependent compressible Euler equations in 3D, extending our previous work on incompressible turbulent flow [16, 17, 18, 19]. For convenience, we use the variables density, velocity and pressure in the a posteriori error analysis. Numerical tests of an adaptive algorithm are presented for test problems in 2D and 3D, for computation of the drag force on different bodies in a flow field. We use a simple finite element method with linear approximation in space and time, and with streamline diffusion stabilization and residual based shock-capturing. This choice of stabilization is a simplified version of GLS and SUPG formulations [20, 21, 22] and shock-capturing [23, 24] of compressible flows. The focus here is the a posteriori error estimation and the adaptive algorithm, which extends to general finite element methods, not just the particular method shown in this paper.

We organize the paper as follows: first we recall the compressible Euler equations, for which we derive an adjoint (dual) problem. We then present a stabilized finite element discretization of both the primal and the dual equations, for which we derive an a posteriori error estimate which forms the basis for an adaptive algorithm. We end with some numerical tests of the adaptive method, and a conclusion and outlook.

2. The Euler equations

The compressible *Euler equations* express conservation of mass, momentum and total energy for an inviscid fluid enclosed in a fixed (open) domain Ω in three-dimensional space $\mathbb{R}^3$ with boundary Γ over a time interval $[0, \hat{t}\,]$ with initial time zero and final time $\hat{t}$.

We seek the *density* ρ, *momentum* $m = \rho u$, with $u = (u_1, u_2, u_3)$ the *velocity*, and the *total energy* e as functions of $(x, t) \in \Omega \cup \Gamma \times [0, \hat{t}\,]$, where $x = (x_1, x_2, x_3)$ denotes the coordinates in $\mathbb{R}^3$ and u_i is the velocity in the x_i-direction. The Euler equations for $\hat{u} \equiv (\rho, m, e)$ read with $Q = \Omega \times I$ and $I = (0, \hat{t}\,]$:

$$\begin{aligned} \dot{\rho} + \nabla \cdot (\rho u) &= 0 && \text{in } Q, \\ \dot{m}_i + \nabla \cdot (m_i u) + p_{,i} &= f_i && \text{in } Q, \quad i = 1, 2, 3, \\ \dot{e} + \nabla \cdot (eu + pu) &= 0 && \text{in } Q, \\ \hat{u}(\cdot, 0) &= \hat{u}_0 && \text{in } \Omega, \end{aligned} \tag{1}$$

where $p = p(x, t)$ is the *pressure* of the fluid, $p_{,i} = \partial p / \partial x_i$ is the partial derivative with respect to x_i, the dot indicates differentiation with respect to time and $f = (f_1, f_2, f_3)$ is a given *volume force* (like gravity) acting on the fluid, and $\hat{u}_0 = \hat{u}_0(x)$ represents initial conditions. Further, the total energy is $e = k + \theta$, where $k = \rho |u|^2 / 2$ is the *kinetic energy*, with $|u|^2 \equiv u_1^2 + u_2^2 + u_3^2$,

and $\theta = \rho T$ is the *internal energy* with T the *temperature* scaled so that $c_v = 1$, where c_v is the heat capacity under constant volume.

The number of unknowns including the pressure is six but there are only five equations in the Euler system (1), and so we close the system with the *state equation* of a *perfect gas*;

$$p = (\gamma - 1)\rho T, \tag{2}$$

expressing the pressure p as a function of density ρ and temperature T, where $\gamma = c_p$ is the *adiabatic index* with c_p the heat capacity under constant pressure, and $(\gamma - 1)$ is the *gas constant*.

For a perfect gas, the *speed of sound* c is given by $c^2 = \gamma(\gamma - 1)T$, and the *Mach number* is defined as $M = |u|/c$.

Here we use different boundary conditions for solving the equations (1): supersonic inflow, subsonic inflow, subsonic outflow and solid wall boundary conditions. For the supersonic case the *characteristics* of the corresponding quasilinear system of (1) are in the direction of flow, so that the Dirichlet boundary conditions for all variables should be imposed at the inflow, whereas no boundary condition is imposed on outflow. In this case all values on the outflow boundary are determined by the interior points.

For the subsonic case we use non-reflecting boundary conditions using *Riemann invariants* or *characteristic variables*, see [25]. The Riemann invariands discribe a variation along the characteristic directions. The idea is that the amplitude of an incoming wave should remain constant for the non-reflecting outflow conditions. This corresponds to putting the variation of Riemann invariants corresponding to incoming waves to zero.

The *slip boundary condition* is imposed at solid wall boundaries, requiring the normal velocity $u \cdot \hat{n}$ with $\hat{n}$ an outward normal of the body, to vanish corresponding to an impenetrable boundary with zero friction.

3. The adjoint operator for the Euler equations

In this section we derive an adjoint operator for the compressible Euler equations. To simplify the derivation we rewrite the equations (1) in the variables: density ρ, velocity $u = (u_1, u_2, u_3)$, and pressure p. Then we linearize the Euler equations with respect to the new variables, for which we derive an adjoint operator. In the rest of this paper we use the Einstein summation convention, where a repeated index indicates summation over that index.

3.1. The Euler equations in terms of density, velocity and pressure

By the relation $m_i = \rho u_i$ and using mass conservation in (1), we can write the conservation of momentum in the following form

$$\rho\left(\dot{u}_i + u_j \frac{\partial u_i}{\partial x_j}\right) + \frac{\partial p}{\partial x_i} = f_i \quad \text{in } Q, \quad i = 1, 2, 3. \tag{3}$$

Next, we derive an equation for the pressure from the conservation of energy. For that, we first formulate an equation for the internal energy, $\theta = \rho T$, by inserting $e = k + \theta$ into the energy equation, and subtracting the equation for kinetic energy $k = \rho\dfrac{u_i u_i}{2}$ we get by taking

the scalar product of the momentum equation with u,

$$\dot{\theta} + \frac{\partial}{\partial x_j}(u_j\theta) + p\frac{\partial u_j}{\partial x_j} = 0. \tag{4}$$

Using the state equation for a perfect gas $p = (\gamma - 1)\rho T$, and by the relation $\theta = \rho T$ we obtain the pressure equation

$$\dot{p} + \frac{\partial}{\partial x_j}(u_j p) + (\gamma - 1)p\frac{\partial u_j}{\partial x_j} = 0. \tag{5}$$

Finally, by collecting the above equations in one system, we obtain a formulation of the Euler equation in terms of density, velocity and pressure: find $\hat{u} = (\rho, u_i, p) \in Q$, such that

$$\begin{aligned}
\dot{\rho} + \frac{\partial}{\partial x_j}(\rho u_j) &= 0 && \text{in } Q, \\
\rho\left(\dot{u}_i + u_j\frac{\partial u_i}{\partial x_j}\right) + \frac{\partial p}{\partial x_i} &= f_i && \text{in } Q, \quad i = 1, 2, 3, \\
\dot{p} + \frac{\partial}{\partial x_j}(u_j p) + (\gamma - 1)p\frac{\partial u_j}{\partial x_j} &= 0 && \text{in } Q, \\
\hat{u}(\cdot, 0) &= \hat{u}_0 && \text{in } \Omega.
\end{aligned} \tag{6}$$

3.2. The linearized Euler equation

Now, consider a linearization of the Euler equations, (6). For simplicity we assume there are no source terms in the equations. Let

$$\begin{aligned}
\rho(x,t) &= \rho_h(x,t) + \tilde{\rho}(x,t), \\
p(x,t) &= p_h(x,t) + \tilde{p}(x,t), \\
u(x,t) &= u_h(x,t) + \tilde{u}(x,t),
\end{aligned} \tag{7}$$

where $\hat{u}_h = (\rho_h, p_h, u_h)$ is the background state, or approximate solution, we linearize at, and $\tilde{\hat{u}} = (\tilde{\rho}, \tilde{p}, \tilde{u})$ is the perturbation, or error. We insert (7) into (6), where we denote higher order terms in $\tilde{\hat{u}}$ by *h.o.t.*, to get the following equations for the perturbation variables:

$$\begin{aligned}
\dot{\tilde{\rho}} + \frac{\partial}{\partial x_j}(\rho_h\tilde{u}_j + \tilde{\rho}u_{h_j}) &= -R_\rho(\hat{u}_h) + h.o.t. && \text{in } Q, \\
\rho_h\left(\dot{\tilde{u}}_i + u_{h_j}\frac{\partial \tilde{u}_i}{\partial x_j} + \tilde{u}_j\frac{\partial u_{h_i}}{\partial x_j}\right) + & \\
\tilde{\rho}\left(\dot{u}_{h_i} + u_{h_j}\frac{\partial u_{h_i}}{\partial x_j}\right) + \frac{\partial \tilde{p}}{\partial x_i} &= -R_{u_i}(\hat{u}_h) + h.o.t. && \text{in } Q, \quad i = 1, 2, 3, \\
\dot{\tilde{p}} + \frac{\partial}{\partial x_j}(u_{h_j}\tilde{p} + \tilde{u}_j p_h) + & \\
(\gamma - 1)\left(p_h\frac{\partial \tilde{u}_j}{\partial x_j} + \tilde{p}\frac{\partial u_{h_j}}{\partial x_j}\right) &= -R_p(\hat{u}_h) + h.o.t. && \text{in } Q, \\
\hat{\tilde{u}}(\cdot, 0) &= \hat{\tilde{u}}_0 && \text{in } \Omega,
\end{aligned} \tag{8}$$

where $R(\hat{u}_h) = (R_\rho(\hat{u}_h), R_{u_i}(\hat{u}_h), R_p(\hat{u}_h)$ are residuals of the Euler equations (6). The system (8), when dropping higher order terms, we denote as the linearized Euler equations (LEE), which models the evolution of small disturbances such as numerical errors.

3.3. Dual problem for LEE

In this section we derive a dual problem for LEE, where we use the following notation for the error:

$$\begin{aligned} e_\rho &= \rho - \rho_h, \\ e_{u_i} &= u_i - u_{h_i}, \quad i = 1,2,3, \\ e_p &= p - p_h. \end{aligned} \tag{9}$$

We assume $\hat{u} = (\rho, u_i, p)$ to be a function in $L_2(I; H^1(\Omega) \times [H^1(\Omega)]^3 \times H^1(\Omega))$ with its time derivative in $L_2(I; L_2(\Omega) \times [L_2(\Omega)]^3 \times L_2(\Omega))$, and $\hat{u}_h = (\rho_h, u_{h_i}, p_h)$ to be a finite element approximation in the corresponding subspace, with standard notation from functional analysis, see [26].

We can then write the LEE as:

$$\begin{aligned} \dot{e}_\rho + \frac{\partial}{\partial x_j}(\rho e_{u_j} + e_\rho u_j) &= -R_\rho(\hat{u}_h) + h.o.t., \\ \rho\left(\dot{e}_{u_i} + u_j\frac{\partial e_{u_i}}{\partial x_j} + e_{u_j}\frac{\partial u_i}{\partial x_j}\right) + e_\rho\left(\dot{u}_i + u_j\frac{\partial u_i}{\partial x_j}\right) + \frac{\partial e_p}{\partial x_i} &= -R_{u_i}(\hat{u}_h) + h.o.t., \\ \dot{e}_p + \frac{\partial}{\partial x_j}(u_j e_p + e_{u_j} p) + (\gamma-1)\left(p\frac{\partial e_{u_j}}{\partial x_j} + e_p\frac{\partial u_j}{\partial x_j}\right) &= -R_p(\hat{u}_h) + h.o.t., \end{aligned} \tag{10}$$

for $i = 1,2,3$, where we have dropped the h-index on the approximate solution $\hat{u}_h$ for simplicity. We can then derive the following dual problem for LEE:

Theorem 1. *Let $\hat{\phi} = (\phi_\rho, \phi_{u_i}, \phi_p) \in L_2(I; H^1(\Omega) \times [H^1(\Omega)]^3 \times H^1(\Omega))$ denote a dual density, velocity and pressure, with $\dot{\hat{\phi}} = (\dot{\phi_\rho}, \dot{\phi_{u_i}}, \dot{\phi_p}) \in L_2(I; L_2(\Omega) \times [L_2(\Omega)]^3 \times L_2(\Omega))$, and let $\hat{n} = (n_1, n_2, n_3)$ be the outward unit normal to the boundary Γ. Assume that the normal components of the primal velocity and dual velocity vanish on the boundary Γ: $u \cdot \hat{n} = \phi_u \cdot \hat{n} = 0$, and that $\hat{\phi}(\cdot, \hat{t}) = 0$ in Ω. If we assume that the error in initial data is zero, i.e. $e(\cdot, 0) = 0$, then we can pose the following dual problem with the left hand side being the adjoint operator of the linearized Euler equation:*

$$\begin{aligned} -\dot{\phi}_\rho - u_j\frac{\partial \phi_\rho}{\partial x_j} + \left(\dot{u}_i + u_j\frac{\partial u_i}{\partial x_j}\right)\phi_{u_i} &= \psi_\rho, && \text{in } Q, \\ -(\dot{\phi_{u_i}}\rho) - \frac{\partial}{\partial x_j}(\rho u_j \phi_{u_i}) + \rho\phi_{u_j}\frac{\partial u_j}{\partial x_i} - p\frac{\partial \phi_p}{\partial x_i} & \\ -(\gamma-1)\frac{\partial}{\partial x_i}(p\phi_p) - \rho\frac{\partial \phi_\rho}{\partial x_i} &= \psi_{u_i}, && \text{in } Q \\ -\dot{\phi}_p - u_j\frac{\partial \phi_p}{\partial x_j} + (\gamma-1)\phi_p\frac{\partial u_j}{\partial x_j} - \frac{\partial \phi_{u_i}}{\partial x_i} &= \psi_p && \text{in } Q, \\ \hat{\phi}(\cdot, \hat{t}) &= 0 && \text{in } \Omega, \end{aligned} \tag{11}$$

for $i = 1,2,3$, where $\psi = (\psi_\rho, \psi_{u_i}, \psi_p) \in L_2(I; L_2(\Omega) \times [L_2(\Omega)]^3 \times L_2(\Omega))$ is data which defines a quantity of interest, and $\hat{t}$ is the final time.

Proof: *We multiply $\hat{\phi} = (\phi_\rho, \phi_{u_i}, \phi_p)$ to the left hand side of the error equation (10), and integrate every term by parts. Note that the boundary terms in time vanish by the assumptions of the theorem. If we let $(v, w) = \int_0^{\hat{t}}\int_\Omega v \cdot w \mathrm{d}x\mathrm{d}t$ denote the $L_2(Q)$-inner product, we get the following relations:*

The error equation for the density:

$$\begin{aligned}\mathrm{I} = &\left(\dot{e}_\rho + \frac{\partial}{\partial x_j}(\rho e_{u_j} + e_\rho u_j), \phi_\rho\right) = \\ &-(e_\rho, \dot{\phi_\rho}) - \left(e_{u_j}, \rho\frac{\partial}{\partial x_j}\phi_\rho\right) + \int_0^T\int_\Gamma \rho e_{u_j} n_j \phi_\rho \mathrm{d}S\mathrm{d}t \\ &-\left(e_\rho, u_j\frac{\partial}{\partial x_j}\phi_\rho\right) + \int_0^T\int_\Gamma e_\rho u_j n_j \phi_\rho \mathrm{d}S\mathrm{d}t.\end{aligned} \tag{12}$$

The error equation for the velocity:

$$\begin{aligned}\mathrm{II} = &\left[\rho\left(\dot{e}_{u_i} + u_j\frac{\partial e_{u_i}}{\partial x_j} + e_{u_j}\frac{\partial u_i}{\partial x_j}\right) + e_\rho\left(\dot{u}_i + u_j\frac{\partial u_i}{\partial x_j}\right) + \frac{\partial e_p}{\partial x_i}, \phi_{u_i}\right] = \\ &-(e_{u_i}, (\dot{\phi_{u_i}\rho})) - \left(e_{u_i}, \frac{\partial}{\partial x_j}(\rho u_j \phi_{u_i})\right) + \int_0^T\int_\Gamma e_{u_i} n_j \rho u_j \phi_{u_i}\mathrm{d}S\mathrm{d}t \\ &+\left(e_{u_j}, \rho\phi_{u_i}\frac{\partial u_i}{\partial x_j}\right) + \left(e_\rho, \left(\dot{u}_i + u_j\frac{\partial u_i}{\partial x_j}\right)\phi_{u_i}\right) \\ &-\left(e_p, \frac{\partial \phi_{u_i}}{\partial x_i}\right) + \int_0^T\int_\Gamma \phi_{u_i} n_i e_p \mathrm{d}S\mathrm{d}t.\end{aligned} \tag{13}$$

The error equation for the pressure:

$$\begin{aligned}\mathrm{III} = &\left[\dot{e}_p + \frac{\partial}{\partial x_j}(u_j e_p + e_{u_j} p) + (\gamma-1)\left(p\frac{\partial e_{u_j}}{\partial x_j} + e_p\frac{\partial u_j}{\partial x_j}\right), \phi_p\right] = \\ &-(e_p, \dot{\phi_p}) - \left(e_p, u_j\frac{\partial \phi_p}{\partial x_j}\right) + \int_0^T\int_\Gamma u_j e_p n_j \phi_p \mathrm{d}S\mathrm{d}t \\ &-\left(e_{u_j}, p\frac{\partial \phi_p}{\partial x_j}\right) + \int_0^T\int_\Gamma e_{u_j} p n_j \phi_p \mathrm{d}S\mathrm{d}t \\ &-(\gamma-1)\left(e_{u_j}, \frac{\partial}{\partial x_j}(p\phi_p)\right) + (\gamma-1)\int_0^T\int_\Gamma e_{u_j} n_j p \phi_p \mathrm{d}S\mathrm{d}t \\ &+(\gamma-1)\left(e_p, \phi_p\frac{\partial u_j}{\partial x_j}\right).\end{aligned} \tag{14}$$

By collecting terms for each error variable e_ρ, e_{u_i}, e_p, we get the dual problem (11):

$$\mathrm{I} + \mathrm{II} + \mathrm{III} = (e_\rho, A^*_{\phi_\rho}(\hat{\phi})) + (e_{u_i}, A^*_{\phi_{u_i}}(\hat{\phi})) + (e_p, A^*_{\phi_p}(\hat{\phi})), \tag{15}$$

where $A^*(\hat{\phi}) = \left(A^*_{\phi_\rho}(\hat{\phi}), A^*_{\phi_{u_i}}(\hat{\phi}), A^*_{\phi_p}(\hat{\phi})\right)$ is the adjoint operator for the linearized Euler equations (10). □

4. A General Galerkin (G2) finite element method

We now introduce a stabilized finite element method, which we here refer to as a General Galerkin or G2 method.

In time, the trial functions are continuous piecewise linear and the test functions are piecewise constant, and in space both test functions and trial functions are continuous piecewise linear.

Let $0 = t_0 < t_1 < ... < t_N = \hat{t}$, be a sequence of discrete time steps with associated time intervals $I_n = (t_{n-1}, t_n]$ of length $\Delta t_n = t_n - t_{n-1}$ and space-time slabs $S_n = \Omega \times I_n$, and let $W_h \subset H^1(\Omega)$ be a finite element space consisting of continuous piecewise linear functions on a fixed mesh $\mathcal{T}_h = \{K\}$ of mesh size $h(x) < 1$, with elements K.

We solve the primal problem for density, momentum and energy, while we solve the dual problem for the dual variables of density, velocity and pressure. The following subsections show finite element discretizations of the equations (1) and (11) using G2.

4.1. G2 for the primal compressible Euler equations

We seek functions $\hat{u}_h = (\rho_h, m_h, e_h)$, continuous piecewise linear in space and time. The G2 method for the compressible Euler equations, here without source terms for simplicity, reads: For $n = 1, ..., N$, find $\hat{u}_h^n = (\rho_n, m_n, e_n) \equiv (\rho_h(t_n), m_h(t_n), e_h(t_n))$ with $\hat{u}_h^n \in V_h \equiv W_h \times W_h^3 \times W_h$, such that

$$
\begin{aligned}
(\dot{\rho}_n, v_n^\rho) - (u_n\bar{\rho}_n, \nabla v_n^\rho) + \int_\Gamma \bar{\rho}_n v_n^\rho u_n \cdot \hat{n}\mathrm{d}S + SD_\rho(\rho_h; v_n^\rho) &= 0, && (16)\\
(\dot{m}_{n_j}, v_{n_j}^m) - (u_n\bar{m}_{n_j}, \nabla v_{n_j}^m) - (p_n, \nabla \cdot v_{n_j}^m) + & \\
\int_\Gamma \bar{m}_{n_j} v_{n_j}^m u_n \cdot \hat{n}\mathrm{d}S + \int_\Gamma p_n v_{n_j}^m \hat{n}_j \mathrm{d}S + SD_{m_j}(m_h; v_{n_j}^m) &= 0, \quad j = 1, 2, 3 && (17)\\
(\dot{e}_n, v_n^e) - (u_n\bar{e}_n, \nabla v_n^e) + (\nabla \cdot (u_n p_n), v_n^e) + & \\
\int_\Gamma \bar{e}_n v_n^e u_n \cdot \hat{n}\mathrm{d}S + SD_e(e_h; v_n^e) &= 0, && (18)
\end{aligned}
$$

for all test functions $\hat{v}_n = (v_n^\rho, v_{n_j}^m, v_n^e) \in V_h$, where

$$
(v, w) = \sum_{K \in \mathcal{T}_h} \int_K v \cdot w \, dx,
$$

with K the cells of the mesh $\mathcal{T}_h$, and

$$
\dot{\rho}_n = \frac{\rho_n - \rho_{n-1}}{\Delta t_n}, \quad \dot{m}_n = \frac{m_n - m_{n-1}}{\Delta t_n}, \quad \dot{e}_n = \frac{e_n - e_{n-1}}{\Delta t_n},
$$

$$
\bar{\rho}_n = \frac{1}{2}(\rho_n + \rho_{n-1}), \quad \bar{m}_n = \frac{1}{2}(m_n + m_{n-1}), \quad \bar{e}_n = \frac{1}{2}(e_n + e_{n-1}),
$$

where we define u_n, p_n and T_n to be finite element functions in W_h^3, W_h and W_h respectively, which are defined by their nodal values given by

$$
\begin{aligned}
u_n(N_i) &= \bar{m}_n(N_i)/\bar{\rho}_n(N_i),\\
p_n(N_i) &= (\gamma - 1)\bar{\rho}_n(N_i)T_n(N_i),\\
T_n(N_i) &= \bar{e}_n(N_i)/\bar{\rho}_n(N_i) - |u_n(N_i)|^2/2
\end{aligned} \qquad (19)
$$

for all nodes N_i in the mesh $\mathcal{T}_h$.

We define a componentwise stabilization in the form of a weighted least squares stabilization of the convection terms together with residual based shock-capturing,

$$SD_\rho(\rho_h; v_n^\rho) = (\delta u_n \cdot \nabla \bar{\rho}_n, u_n \cdot \nabla v_n^\rho) + (\hat{\nu}_\rho \nabla \bar{\rho}_n, \nabla v_n^\rho), \quad (20)$$

$$SD_{m_j}(m_h; v_{n_j}^m) = (\delta u_n \cdot \nabla \bar{m}_{n_j}, u_n \cdot \nabla v_{n_j}^m) + (\hat{\nu}_m \nabla \bar{m}_{n_j}, \nabla v_{n_j}^m), \quad j = 1, 2, 3 \quad (21)$$

$$SD_e(e_h; v_n^e) = (\delta u_n \cdot \nabla \bar{e}_n, u_n \cdot \nabla v_n^e) + (\hat{\nu}_e \nabla \bar{e}_n, \nabla v_n^e), \quad (22)$$

where $\delta = C_\delta(\Delta t_n^{-2} + |u_n|^2 h^{-2})^{-1/2}$ and $\hat{\nu}_\alpha = \max(C_\alpha \frac{|R_\alpha(\hat{u})|}{|\alpha_h|} h^2, C_h h^{3/2})$, for $\alpha = \rho, m, e$, and $\alpha_h = \rho_h, m_h + \epsilon, e_h$, with $\epsilon > 0$ a small safety factor, and with constants C_δ, C_α and $C_h \sim \frac{U}{\sqrt{L}}$, where U and L are characteristic velocity and length scales of the problem, and we define the residuals for $t \in I_n$ by

$$R_\rho(\hat{u}_h) = \dot{\rho}_n + \nabla \cdot (\bar{\rho}_n u_n), \quad (23)$$

$$R_{m_j}(\hat{u}_h) = (\dot{m}_n)_j + \nabla \cdot ((\bar{m}_n)_j u_n) + \partial p_n / \partial x_j, \quad j = 1, 2, 3, \quad (24)$$

$$R_e(\hat{u}_h) = \dot{e}_n + \nabla \cdot (\bar{e}_n u_n + p_n u_n). \quad (25)$$

The method (16) - (18) is a simple stabilized finite element method, with only a least squares stabilization of the convection term and a shock capturing term based on the individual residuals of each equation. The method conserves mass, momentum and energy, and results in a symmetric stabilization matrix in the discrete system. As it has been mentioned, the method with above stabilization and shock-capturing parameters is a simplified version of SUPG and GLS methods. The choice of stabilization and shock-capturing parameters is an active focus of research over the last decades. For an overview of the resent development of stabilized finite element methods and the choice of stabilization parameters see e.g. [27, 28, 29, 30, 31].

We solve the discretized equations by a fixed-point iteration with velocity given from the previous iteration, resulting in a linear system which we solve by GMRES. With this method the time step Δt_n is given by a CFL-condition, with typically $\Delta t_n \sim \min_{K \in \mathcal{T}_h}(h/|u_n|)_K$.

We remark that the a posteriori error analysis in this paper extends to general stabilized finite element methods with small modifications.

4.2. G2 for the dual linearized Euler equations

The a posteriori error estimate in this paper is given in terms of the solution to a continuous dual problem, but this dual solution is in general unavailable, and thus discrete approximations are needed.

As for the primal problem, we seek functions $\hat{\phi}_h = (\phi_\rho, \phi_{u_i}, \phi_p)$, continuous piecewise linear in space and time, with $n = 1, \cdots, N$ and $i = 1, 2, 3$: find $\hat{\phi}_h^n = (\phi_{\rho_n}, \phi_{u_{n_i}}, \phi_{p_n}) = (\phi_\rho(t_n), \phi_{u_i}(t_n), \phi_p(t_n)) \in V_{h,g} = \{v : v \in W_h \times W_h^3 \times W_h, v|_\Gamma = g\}$, such that

$$
\begin{aligned}
-(\dot{\phi}_{\rho_n}, v_n^\rho) - \left(u_{n_j}\frac{\partial\bar{\phi}_{\rho_n}}{\partial x_j}, v_n^\rho\right) + \left(\left(\dot{u}_{n_j} + u_{n_j}\frac{\partial u_{n_j}}{\partial x_j}\right)\bar{\phi}_{u_{n_i}}, v_n^\rho\right) & \\
+\nu_h\left(\frac{\partial\bar{\phi}_{\rho_n}}{\partial x_j}, \frac{\partial v_n^\rho}{\partial x_j}\right) &= (\psi_{\rho_n}, v_n^\rho), \qquad (26)\\
-\left(\dot{\phi}_{u_{n_i}}\rho_n, v_{n_i}^u\right) + \left(\rho_n u_{n_j}\bar{\phi}_{u_{n_i}}, \frac{\partial v_{n_i}^u}{\partial x_j}\right) + \left(\rho_n\bar{\phi}_{u_{n_j}}\frac{\partial u_{n_j}}{\partial x_i}, v_{n_i}^u\right) & \\
-\left(p_n\frac{\partial\bar{\phi}_{p_n}}{\partial x_i}, v_{n_i}^u\right) - \left(\rho_n\frac{\partial\bar{\phi}_{\rho_n}}{\partial x_i}, v_{n_i}^u\right) & \\
+(\gamma-1)\left(p_n\bar{\phi}_{p_n}, \frac{\partial v_{n_i}^u}{\partial x_i}\right) + \nu_h\left(\frac{\partial\bar{\phi}_{u_{n_i}}}{\partial x_j}, \frac{\partial v_{n_i}^u}{\partial x_j}\right) &= (\psi_{u_{n_i}}, v_{n_i}^u), \qquad (27)\\
-(\dot{\phi}_{p_n}, v_n^p) - \left(u_{n_j}\frac{\partial\bar{\phi}_{p_n}}{\partial x_j}, v_n^p\right) + (\gamma-1)\left(\bar{\phi}_{p_n}\frac{\partial u_{n_j}}{\partial x_j}, v_n^p\right) & \\
+\nu_h\left(\frac{\partial\bar{\phi}_{p_n}}{\partial x_j}, \frac{\partial v_n^p}{\partial x_j}\right) + \left(\phi_{u_{n_i}}, \frac{\partial v_n^p}{\partial x_i}\right) &= (\psi_{p_n}, v_n^p), \qquad (28)
\end{aligned}
$$

for all test functions $\hat{v}_n = (v_n^\rho, v_{n_i}^u, v_n^p) \in \hat{V}_{h,0} = \{v : v \in W_h \times W_h^3 \times W_h, v|_\Gamma = 0\}$, where $\hat{\psi}_n = (\psi_n^\rho, \psi_{n_i}^u, \psi_n^p) \in L_2(I; L_2(Q) \times L_2(Q)^3 \times L_2(Q))$ defines a quantity of interest, and ν_h is artificial viscosity. In the computations in this paper we use artificial viscosity $\nu_h = h$. As above, a dot denotes the time derivative in I_n, and a bar denotes the mean value.

The function $\hat{u}_n = (\rho_n, u_n, p_n) \in V_h$ is a computational approximation of the primal solution at time t_n, where the corresponding time derivative is defined as $\dot{u}_n \equiv (u_n - u_{n-1})/\Delta t_n$.

5. An a posteriori error estimate

We introduce the following notation for the a posteriori error analysis:

$$
\begin{aligned}
&(u,w)_K = \int_K v\cdot w\mathrm{d}x, \quad (u,w)_{\partial K} = \int_{\partial K} v\cdot w\mathrm{d}s, \quad (u,w) = \sum_K (u,w)_K,\\
&\|v\|_K = \|v\|_{L_2(K)} = (v,v)_K^{1/2}, \quad |v|_K = (\|v_1\|_K, \|v_2\|_K, \|v_3\|_K), \qquad (29)\\
&I = \bigcup_{n=1}^N I_n, \quad \mathcal{T}_h = \bigcup_{K\in\mathcal{T}_h} K.
\end{aligned}
$$

Assume $\hat{u}_h = (\rho_n, u_{n_i}, p_n) \in V_h$ for $i = 1,2,3$ to be an approximate solution of the equation (6), with corresponding residuals $R(\hat{u}_h) = (R_\rho(\hat{u}_h), R_{u_i}(\hat{u}_h), R_p(\hat{u}_h))$, defined by

$$
\begin{aligned}
R_\rho(\hat{u}_h) &= \dot{\rho}_n + \frac{\partial}{\partial x_j}(\rho_n u_{n_j}), \qquad (30)\\
R_{u_i}(\hat{u}_h) &= \rho_n\left(\dot{u}_{n_i} + u_{n_j}\frac{\partial u_{n_i}}{\partial x_j}\right) + \frac{\partial p_n}{\partial x_i}, \qquad (31)\\
R_p(\hat{u}_h) &= \dot{p}_n + \frac{\partial}{\partial x_j}(u_{n_j}p_n) + (\gamma-1)p\frac{\partial u_{n_j}}{\partial x_j}, \qquad (32)
\end{aligned}
$$

where $i = 1, 2, 3$, and we define time derivatives of density, velocity and pressure as in section 4.2.

Then, the following theorem expresses an error representation for the compressible Euler equations.

Theorem 2. *Assume for $i = 1, 2, 3$, that $\hat{\phi} = (\phi_\rho, \phi_{u_i}, \phi_p)$ is a solution of the dual problem (11), let $\psi = (\psi_\rho, \psi_{u_i}, \psi_p)$ be a quantity of interest $M(\hat{u}) = (\hat{u}, \hat{\psi})$, and let $\pi_h\hat{\phi} = (\pi_h\phi_\rho, \pi_h\phi_{u_i}, \pi_h\phi_p) \in V_h$ denote an interpolant in the finite element space V_h. Then, for an exact solution $\hat{u}$ satisfying (6) and an approximate solution $\hat{u}_h$ computed from (16)-(19), we have the following error representation formula:*

$$\begin{aligned} M(\hat{u}) - M(\hat{u}_h) = &\int_I \sum_{K\in\mathcal{T}_n} \left(-R(\hat{u}_h), \hat{\phi} - \pi_h\hat{\phi}\right)_K \mathrm{d}t \\ &- \int_I \sum_{K\in\mathcal{T}_n} SD([\rho_h, m_h, e_h]; \pi_h\hat{\phi})_K \mathrm{d}t + h.o.t., \end{aligned} \tag{33}$$

where $SD([\rho_h, m_h, e_h]; w) = (SD_\rho(\rho_h; w_\rho), SD_{m_i}(m_h; w_{m_i}), SD_e(e_h; w_e))$, for $w \in V_h$ and $i = 1, 2, 3$.

Proof: *Using (9) and (11), we get*

$$\begin{aligned} M(\hat{u}) - M(\hat{u}_h) &= \int_I (e, \hat{\psi})\mathrm{d}t = \int_I (e_\rho, \psi_\rho)\mathrm{d}t + \int_I (e_{u_i}, \psi_{u_i})\mathrm{d}t + \int_I (e_p, \psi_p)\mathrm{d}t \\ &= \int_I (e_\rho, A^*_{\phi_\rho}(\hat{\phi}))\mathrm{d}t + \int_I (e_{u_i}, A^*_{\phi_{u_i}}(\hat{\phi}))\mathrm{d}t + \int_I (e_p, A^*_{\phi_p}(\hat{\phi}))\mathrm{d}t, \end{aligned} \tag{34}$$

which is nothing other than the relation (15) from the proof of Theorem 1, and by repeating the same steps backwards (integration by parts) we get that

$$M(\hat{u}) - M(\hat{u}_h) = \int_I (A_\rho(e_\rho), \phi_\rho)\mathrm{d}t + \int_I (A_{u_i}(e_{u_i}), \phi_{u_i})\mathrm{d}t + \int_I (A_p(e_p), \phi_p)\mathrm{d}t, \tag{35}$$

with $A = (A_\rho, A_{u_i}, A_p)$ the linearized operator of the left hand side of (8). The relation of the error and residual is expressed in (8) as $A(e) = -R(\hat{u}_h) + h.o.t.$. Using this relation and the G2 method for the primal problem with test function $\hat{v} = \pi_h\hat{\phi}$ we finally get

$$\begin{aligned} M(\hat{u}) - M(\hat{u}_h) &= \int_I (A(e), \hat{\phi})\mathrm{d}t = \int_I (-R(\hat{u}_h) + h.o.t., \hat{\phi})\mathrm{d}t \\ &= \int_I (-R(\hat{u}_h), \hat{\phi} - \pi_h\hat{\phi})\mathrm{d}t - \int_I (SD([\rho_h, m_h, e_h], \pi_h\hat{\phi})\mathrm{d}t + h.o.t.. \quad \square \end{aligned} \tag{36}$$

Now we present the main theorem of the paper, an *a posteriori error estimate of the compressible Euler equation for the G2 method.*

Theorem 3. *Let $\hat{u} = (\rho, u_i, p)$ be a solution of (6) and $\hat{u}_h = (\rho_h, u_{h_i}, p_h)$ an approximation computed from (16)-(19), and let $D\hat{\phi}$ denote first order derivatives of $\hat{\phi}$, with $\hat{\phi} = (\phi_\rho, \phi_{u_i}, \phi_p)$ the solution of the dual problem (11), then we have the following a posteriori error estimate:*

$$\begin{aligned} &|M(\hat{u}) - M(\hat{u}_h)| \leq \\ &\int_I \sum_{K\in\mathcal{T}_n} C_n h |R(\hat{u}_h)|_K \cdot |D\hat{\phi}|_K \mathrm{d}t + \int_I \sum_{K\in\mathcal{T}_n} |SD([\rho_h, m_h, e_h]; \pi_h\hat{\phi})|\mathrm{d}t + h.o.t. \end{aligned} \tag{37}$$

where $SD([\rho_h, m_h, e_h]; w) = (SD_\rho(\rho_h; w), SD_{m_i}(m_h; w), SD_e(e_h; w))$*, for* $w \in V_h$*, is the stabilization term in (16).*

Proof: *We start from the result of Theorem 2. The by using a standard interpolation error estimate of the form* $\|h^{-1}(\hat{\phi} - \pi\hat{\phi})\|_K \leq C_n \|D\phi\|_K$*, we get:*

$$
\begin{aligned}
&|M(\hat{u}) - M(\hat{u}_h)| = \\
&\quad |\int_I \sum_{K\in\mathcal{T}_n} (-R(\hat{u}_h), \hat{\phi} - \pi_h\hat{\phi})\mathrm{d}t - \int_I \sum_{K\in\mathcal{T}_n} SD([\rho_h, m_h, e_h]; \pi_h\hat{\phi})\mathrm{d}t| + h.o.t. \\
&\quad \leq |\int_I \sum_{K\in\mathcal{T}_n} (-R(\hat{u}_h), \hat{\phi} - \pi_h\hat{\phi})\mathrm{d}t| + |\int_I \sum_{K\in\mathcal{T}_n} SD([\rho_h, m_h, e_h]; \hat{\phi}_h)\mathrm{d}t| + h.o.t. \\
&\quad \leq \int_I \sum_{K\in\mathcal{T}_n} |(-R(\hat{u}_h), \hat{\phi} - \pi_h\hat{\phi})|\mathrm{d}t + \int_I \sum_{K\in\mathcal{T}_n} |SD([\rho_h, m_h, e_h]; \pi_h\hat{\phi})|\mathrm{d}t + h.o.t. \\
&\quad \leq \underbrace{\int_I \sum_{K\in\mathcal{T}_n} C_n h |R(\hat{u}_h)|_K \cdot |D\hat{\phi}|_K + \int_I \sum_{K\in\mathcal{T}_n} |SD([\rho_h, m_h, e_h]; \pi_h\hat{\phi})|\mathrm{d}t + h.o.t.}_{\sum_{n,K} \eta_n^K} . \quad \square
\end{aligned}
\tag{38}
$$

We denote η_n^K an error indicator to element K in I_n, $S = \int_I \sum_K |D\hat{\phi}|_K \mathrm{d}t$ a stability factor. The stability factor measures output sensitivity of the quantity of interest for the problem.

6. An adaptive algorithm

In the adaptive algorithm of this paper the mesh, $\mathcal{T}_h$ does not change in time, but remains the same over the whole time interval. First we solve the approximate primal problem forward in time, and then we solve the discretized dual equation backward in time. Based on the posteriori error estimate (37) the mesh is then adaptively refined to reduce the error in the output of interest. The local mesh refinement is based on the *Rivara recursive bisection algorithm*, see [32]. First this algorithm bisects the longest edge, then recursively repeats the bisection of the neighboring triangles of the edge containing the hanging node until this edge is a common longest edge of a cell. To enhance the quality of the refined mesh we combine bisection with Laplacian mesh smoothing.

The timestep is calculated from the smallest cell diameter, with typically $\Delta t_n \sim \min_{K\in\mathcal{T}_h}(h/|u_n|)_K$, for all elements K in the mesh $\mathcal{T}_h$ and the velocity u_n.

Algorithm 1. *Given a tolerance* TOL*, start from an initial coarse mesh* $\mathcal{T}_h^0$*, with* $k = 0$*:*

1. *Compute an approximation to the the primal solution* $\hat{u}_h \in V_h$*, on the current mesh* $\mathcal{T}_h^k$*;*
2. *Compute an approximation of the dual solution* $\hat{\phi}_h \in V_h$*, on the same mesh;*
3. *Compute the error indicator defined in (37), if* $|\sum_{n,K} \eta_n^K| <$ TOL*, then* STOP*;*
4. *Refine a fixed fraction of cells in* $\mathcal{T}_h^k$ *with largest error indicator to get a new mesh* $\mathcal{T}_h^{k+1}$*;*

5. Set $k = k + 1$ and go to 1.

Remark 1. *In this paper we use an approximation of the error indication η_n^K, where the dual solution $\hat{\phi}$ is approximated using the G2 method and the stabilization and high order terms are dropped.*

7. Numerical Examples

We now illustrate Algorithm 1, for compressible fluid flow around an object in 2D and 3D for different Mach numbers, where the quantity of interest is the drag force on the object.

In the simulations we use dimensionless variables: If L is a characteristic length for the problem, then we normalize the density ρ^*, sound speed c^* and the temperature T^*, by their free stream values $\rho_\infty^*, c_\infty^*$ and T_∞^*, and we use non-dimensionalized time $t = L/c_\infty^*$, pressure $p = \frac{p^*}{\rho_\infty^* c_\infty^2}$, and velocity $u = \frac{u^*}{c_\infty}$.

We use the following boundary conditions for the primal equations: for the supersonic case, at the inlet all variables of the solution are given by Dirichlet boundary conditions, at the outlet no boundary condition is imposed. For the transonic case momentum and energy boundary conditions are imposed at the inlet, and after solving the corresponding linear system all variables at the outlet and density at the inlet are corrected by the Riemann invariants for the Euler equations, see e.g. [25]. A slip boundary condition is used in the rest of the computational domain.

For the dual equations we use homogeneous Dirichlet boundary conditions for density and pressure, and for the dual velocity we set $\phi_{u_1}(x,t) = -1$ for all $x \in \Gamma_{body}$, and $\phi_{u_i}(x,t) = 0$ elsewhere for $i = 1, 2, 3$.

7.1. Computation of drag

We compute the drag coefficient as:

$$C_{pd} = \frac{F_{pd}}{1/2\rho_\infty |u_\infty|^2 A}, \tag{39}$$

with F_{pd} a drag force, ρ_∞ the free stream density and u_∞ the free stream velocity of the fluid, and A is a reference area. Typically, the reference area A is a projected area perpendicular to the direction of the fluid.

Since our model is an inviscid compressible fluid the drag force is computed only from the pressure, whereas shear stress due to friction is not included.

The drag force F_{pd} is computed from a surface integral on the body Γ_{body} of the pressure p and an outward (from the fluid domain) unit normal vector n, projected in the direction e_{pd} of the drag:

$$F_{pd} = \int_{\Gamma_{body}} p\hat{n} \cdot e_{pd} \mathrm{d}s. \tag{40}$$

7.2. Supersonic 2D flow around a cylinder

We now consider a compressible supersonic flow around a cylinder with diameter $d = 0.0254$, and with $M = 1.4$ at the inlet. We run the simulation until a time $t = 0.5$ to observe the

behavior of the adaptive algorithm. Note, that this is not a stationary solution to the problem at this time. We plot the solution which is obtained after eleven adaptive mesh refinements with respect to the error in drag. In the a posteriori error estimate of Theorem 3, derivatives of the dual solution act as weights for the local errors in the form of residuals, characterizing sensitivities of the output of interest (here drag) with respect to local errors. Figure 1 shows the solution of the dual problem at time $t = 0.35$ together with the sonic contour $M = 1$ at time $t = 0.5$. The shock waves in the Euler equations develop along the sonic contour, and we find that the dual solution indicates the upstream region, close to the supersonic region, and the downstream region where the wake will develop, to be important for accuracy in drag. However, the residuals of the primal equations are small close to the inlet, but large along the shock wave and the wake.

In Algorithm 1 error indicators η_n^K are computed for each cell K_n of the triangulation $\mathcal{T}_h$, of which a certain fraction are marked for refinement based on the size of the error indicators. Output from the adaptive algorithm is presented in Table I. Figure 2 shows the drag coefficient C_{dp} for a set of adaptive iterations, together with a reference C_{dp}^{ref} which is obtained from a uniformly refined mesh with 115 718 vertices and 230 852 cells. After seven adaptive iterations the drag oscillates about the reference value for drag, and the error estimate $\sum_{n,K} \eta_n^K$ is steadily decreasing, see Figure 3.

Table I. The convergence history of the drag coefficient. Here $\bar{C}_{dp}$ is a mean value of C_{dp} over the time interval $[0, t]$, $C_{dp}^{ref} = 1.3970$ is a reference drag coefficient obtained from a fine uniformly refined mesh, and $\sum_{n,K} \eta_n^K$ denotes a sum of error indicators over the cells.

#iter	#vertices	#cells	S	$\bar{C}_{dp}$	$\sum_{n,K} \eta_n^K$	$\bar{C}_{dp}/\bar{C}_{dp}^{ref}$
0	14660	28792	1.76	1.3217	2.3573	0.9461
1	16176	31824	1.9138	1.3056	1.9317	0.9346
2	17828	35115	2.3296	1.2681	0.9903	0.9077
3	19667	38793	2 1967	1.3742	0.7426	0.9837
4	21716	42888	3.1018	1.3672	0.5653	0.9786
5	24017	47482	3.5975	1.4238	0.3730	1.0191
6	26584	52600	4.2220	1.3640	0.2927	0.9764
7	29557	58530	4.7777	1.4453	0.1923	1.0345
8	32885	65154	5.4866	1.4090	0.1521	1.0086
9	36662	72676	6.0550	1.4438	0.1291	1.0335
10	40962	81213	6.6479	1.4378	0.0939	1.0292
11	46040	91312	7.2120	1.4507	0.0828	1.0385

7.3. Supersonic 2D flow around a wedge

In this example we simulate supersonic $M = 3$ flow around a wedge. Consider a sharp angle wedge at zero angle of attack in Figure 5. One important feature of this flow is that the oblique shock here is attached to the wedge, however for the cylinder there is a detached bow shock, see Figure 1. Also, downstream of the wedge, the shock-expansion waves develops at the sharp

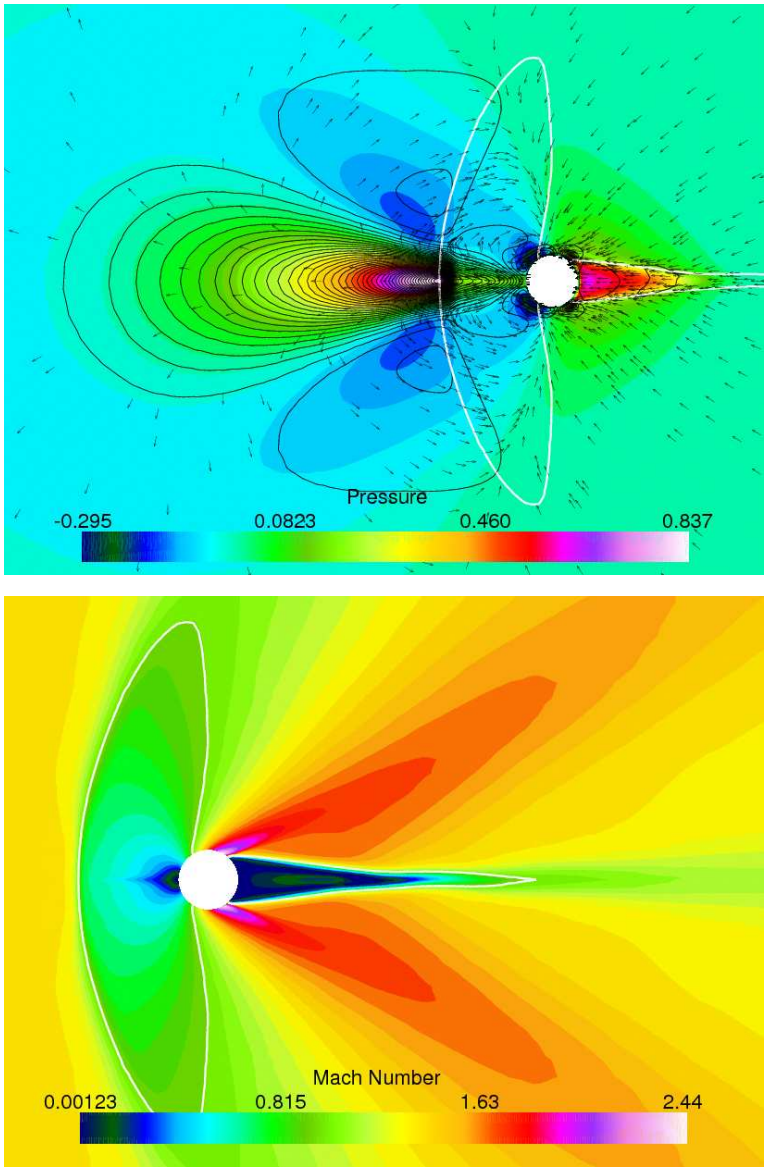

Figure 1. Supersonic flow around a 2D cylinder: the pressure in the colors, density contours and velocity arrow at time $t = 0$ together with the sonic contour $M = 1$ at time $t = 0.5$, *(upper)*. The Mach number at time $t = 0.5$, *(lower)*.

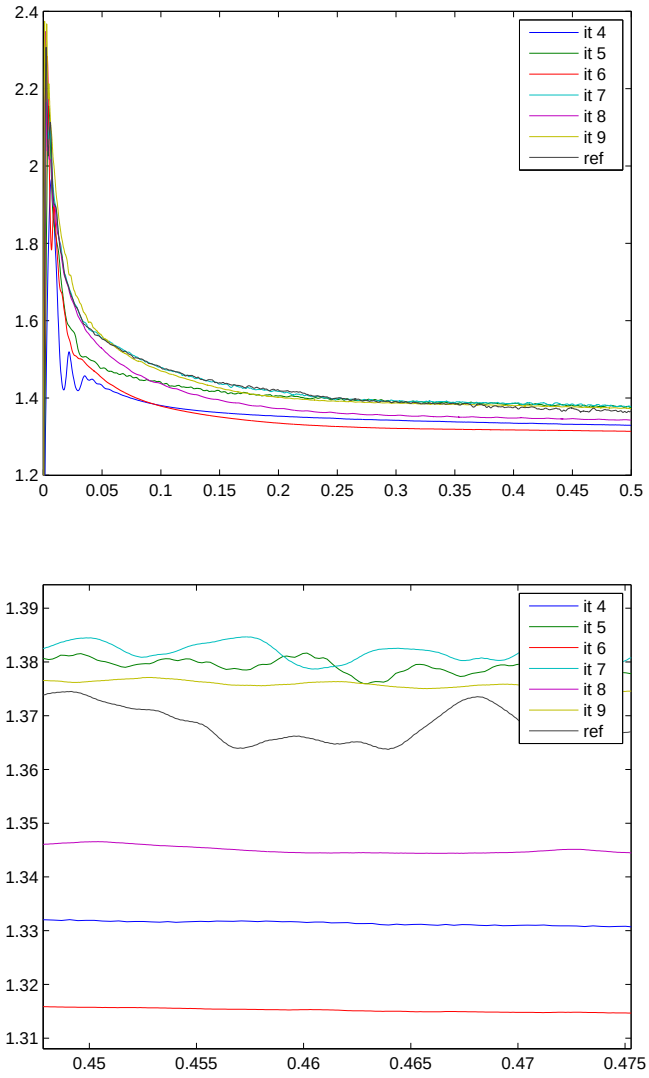

Figure 2. Supersonic flow around a 2D cylinder: the drag coefficient C_{dp} in different adaptive iterations and the reference C_{dp} which is obtained from the reference mesh.

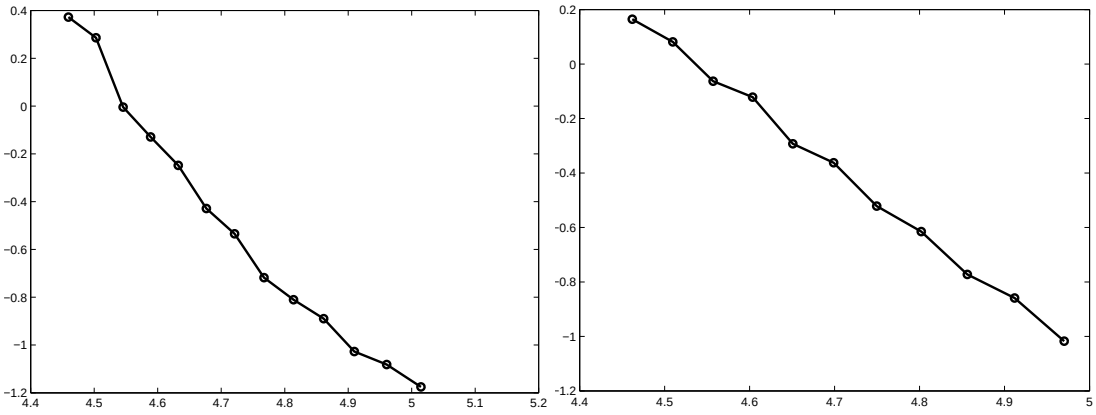

Figure 3. Supersonic flow around a 2D cylinder *(left)* and 2D wedge *(right)*: Log10 of number of cells versus log10 of $\sum_n \eta_n$.

edges.

The boundary conditions are chosen the same as for the cylinder above, with just a higher Mach number at the inlet. There is no special treatment of the corners of the wedge, resulting in a pollution effect close to the body and downstream. This effect vanishes with sufficient mesh refinement, and we find that the adaptive algorithm focuses to these singularity points.

We compare the adaptively refined meshes to two reference drag coefficients from uniformly refined meshes: $C_{dp}^{ref_1}$ obtained from a mesh with 91 074 vertices and 181 844 cells, and $C_{dp}^{ref_2}$ obtained from a mesh with 144 086 vertices and 287 740 cells. However, we find that the drag coefficients obtained from the two uniformly refined meshes are not close to each other, probably due to insufficient mesh refinement near the singularity point at the tip of the wedge. Figure 9 shows the triangulations close to the tip. The left plot is the result of the adaptive algorithm after eight iterations with 41 067 vertices and 81 112 cells and the right plot is the triangulation for the finest uniformly refined mesh. We see that the adaptive algorithm focuses to resolve the singularity point, which makes the pollution effect smaller. Figure 6 shows the drag coefficients from the adapted mesh together with the reference drag coefficients, where we find that drag for the finest uniformly refined mesh is closer to the results from the adapted mesh. We summarized the computational results in Table II, with drag for the adaptively refined meshes quite close for the finer meshes.

Figure 7 shows the dual and primal solutions at time $t = 0$ and $t = 0.5$ respectively. The upper figure shows the dual pressure in color, dual density contours and dual velocity arrows together with 10 contours of the Mach number. We see that the oblique shock is attached to the wedge, it starts from the tip and develops downstream. From the downstream edges, the shock expansion appears. The dual density follows the oblique shock a while and then advects upstream. All dual solutions are focused on the area close to the tip, and the wake which develops after the wedge. The residual is typically high along the shock waves, however for the regions far from the wedge the dual solution is almost zero. This indicates that for accurate approximation the drag force, it is not important to resolve the parts of the domain with very small dual solution. This significantly reduces the computational cost of the simulation. We

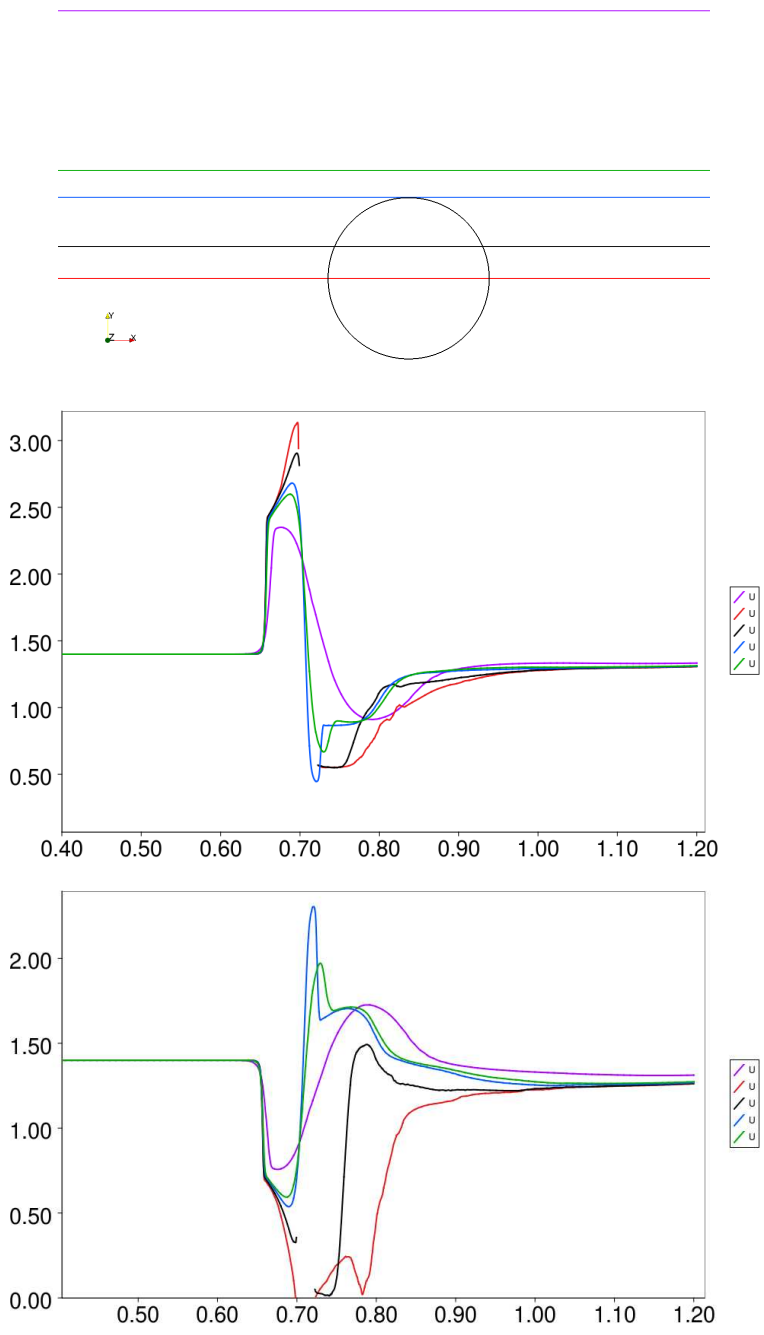

Figure 4. Supersonic flow around a 2D cylinder with $d = 0.0254$: variation of the density *(middle)* and Mach number *(below)* along the x-axis for several y-values from 14 times adaptively refined mesh with 46040 vertices and 91312 cells at time $t = 0.5$: y=0.508 *(red)*; y=0.513 *(black)*; y=0.520721 *(blue)*; y=0.525 *(green)*; y=0.55 *(purple)*.

show the resulting meshes from the adaptive algorithm in Figure 10, both for the 2D cylinder and the wedge. In both examples, the algorithm refines only the part of the shock region which has significant effect on the drag force. Morover, the adaptive algorithm controls the formation of spurious numerical oscillations in the solution. This can be observed in Figures 4 and 8, where we plot the variation of the solution along the x-axis for several y-values from the finest adaptivly refined meshes for both 2D examples.

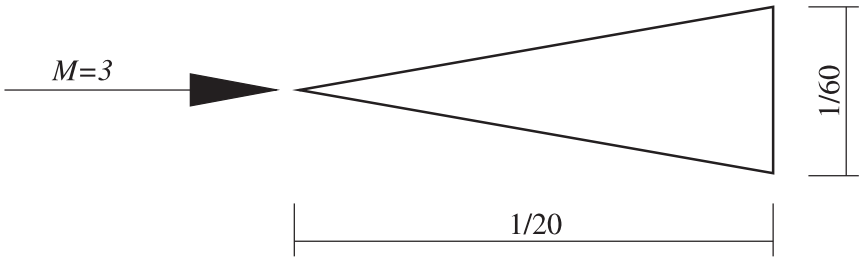

Figure 5. The geometry of the two dimensional wedge.

Table II. The convergence history of a drag coefficient for the Mach 3 flow around a wedge. Here $\bar{C}_{dp}$ is a mean value of C_{dp} over the time interval $[0,t]$, $C_{dp}^{ref_1} = 0.2874$ is a reference drag coefficient from obtained from the fine mesh with 91 074 vertices and 181 844 cells, $C_{dp}^{ref_2} = 0.2616$ is a reference drag coefficient from the finest mesh with 144 086 vertices and 287 740 cells, and $\sum_{n,K} \eta_n^K$ denotes a sum of error indicators of cells.

#iter	#vertices	# cells	S	$\bar{C}_{dp}$	$\sum_{n,K} \eta_n^K$	$\bar{C}_{dp}/\bar{C}_{dp}^{ref_1}$	$\bar{C}_{dp}/\bar{C}_{dp}^{ref_2}$
0	14632	28972	4.5182	0.4333	1.4614	1.5078	1.6565
1	16321	32334	4.9313	0.3838	1.2059	1.3355	1.4672
2	18194	36061	5.1899	0.3445	0.8651	1.1985	1.3167
3	20250	40141	6.0702	0.2576	0.7564	0.8962	0.9846
4	22579	44759	6.1874	0.2476	0.5094	0.8616	0.9466
5	25225	49989	7.1764	0.2490	0.4341	0.8663	0.9517
6	28356	56172	7.3092	0.2490	0.0316	0.8664	0.9518
7	32019	63380	8.3547	0.2495	0.0254	0.8680	0.9536
8	36312	71820	8.5274	0.2522	0.0177	0.8777	0.9643
9	41305	81621	9.7619	0.2524	0.0145	0.8784	0.9650
10	47345	93374	12.913	0.2542	0.0100	0.8844	0.9716

8. Supersonic 3D flow around a sphere

Experimental data for compressible flow around a sphere for different Mach numbers and Reynolds numbers are available over the number of publications starting from the 18th century.

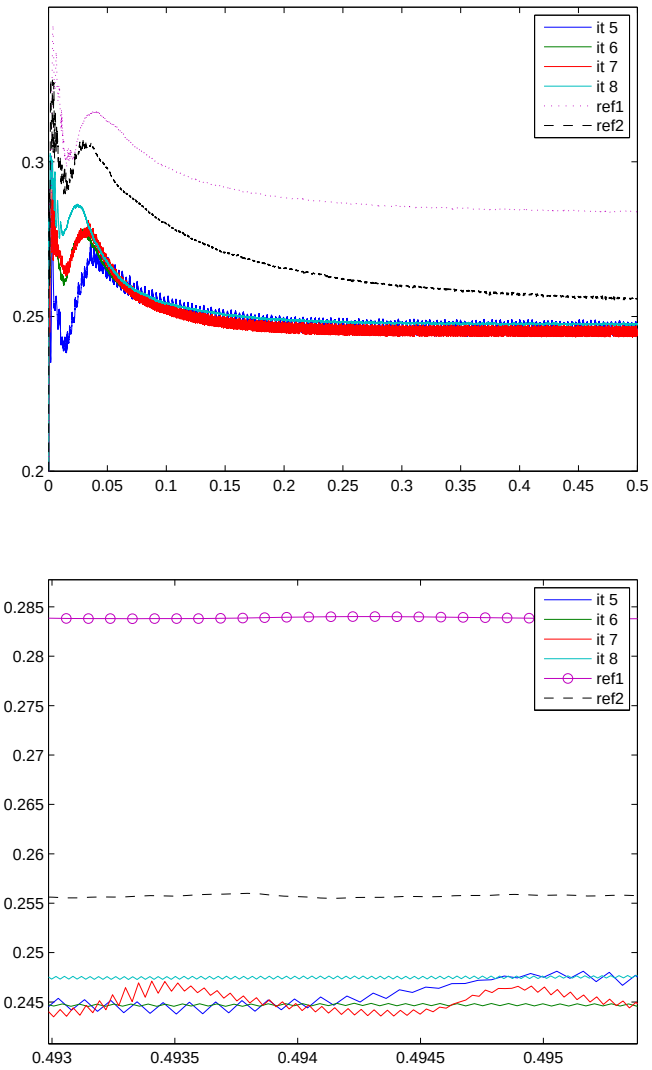

Figure 6. Supersonic flow around a 2D wedge: the drag coefficient C_{dp} in different adaptive iterations and two reference coefficients $C_{dp}^{ref_1}$ and $C_{dp}^{ref_2}$.

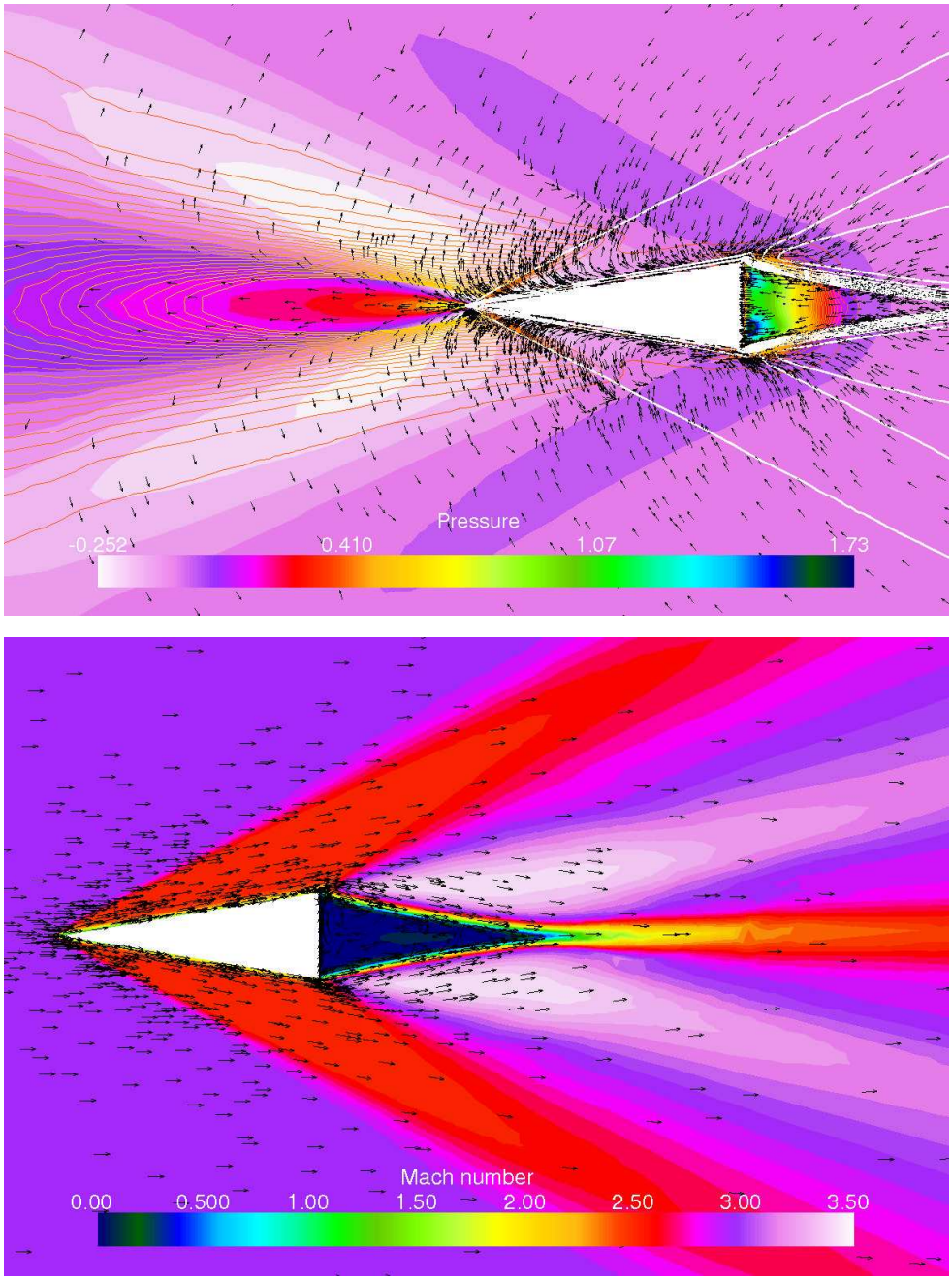

Figure 7. Supersonic flow around a 2D wedge: the dual pressure in the colors, dual density contours and velocity arrow at time $t = 0$ together with 10 contour of Mach numbers at time $t = 0.5$, *(upper)*. The Mach number at time and primal velocity arrows $t = 0.5$, *(lower)*.

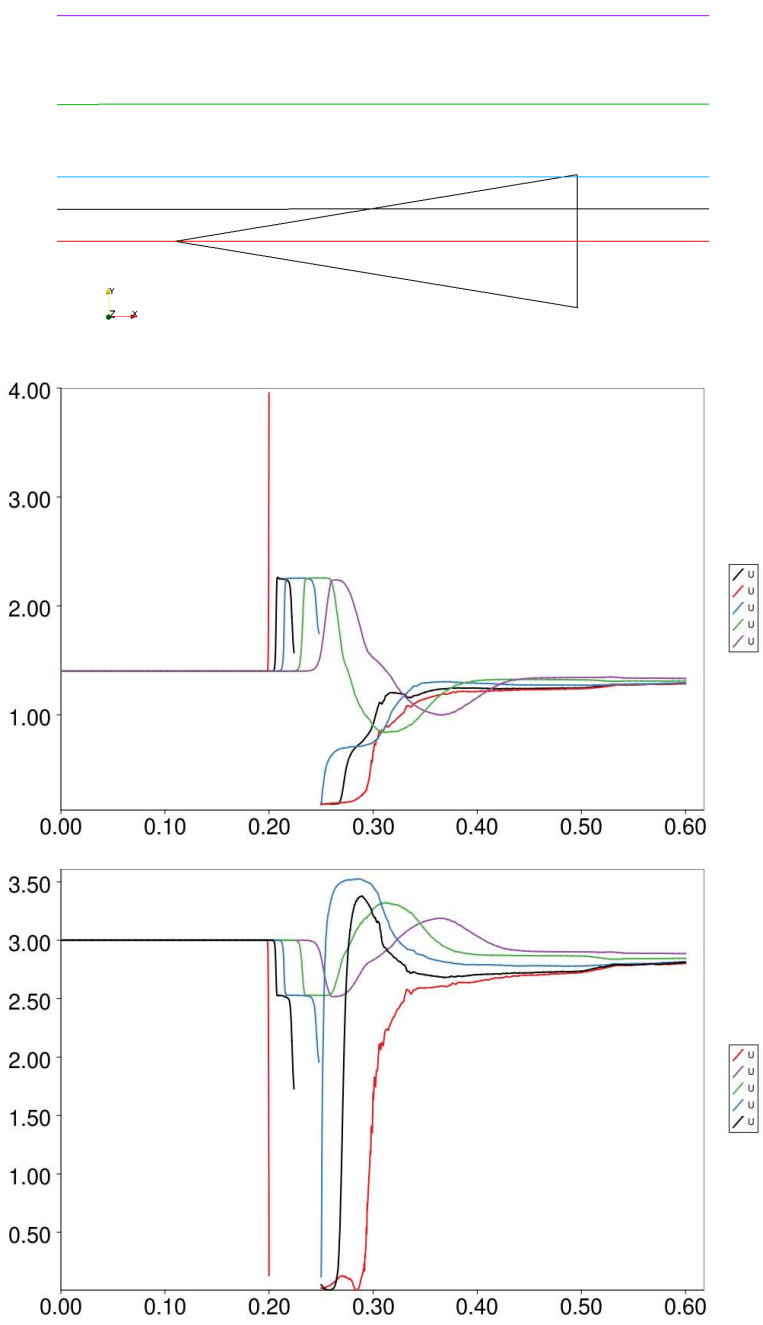

Figure 8. Supersonic flow around a 2D wedge with length 0.05 in the x direction: variation of the density *(middle)* and Mach number *(below)* along the x-axis for several y-values from 10 times adaptively refined mesh with 47345 vertices and 93374 cells at time $t = 0.5$: y=0.2 *(red)*; y=0.204 *(black)*; y=0.208 *(blue)*; y=0.217 *(green)*; y=0.228 *(purple)*.

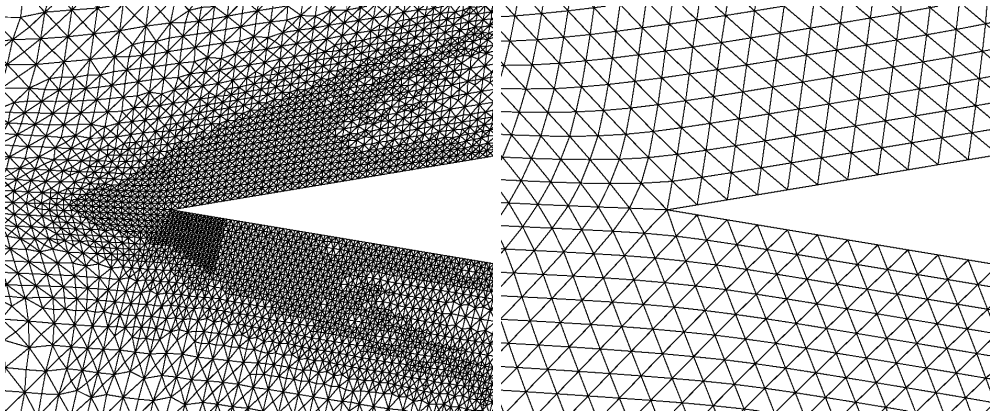

Figure 9. Supersonic flow around a 2D wedge: the mesh close to the tip of the wedge: after nine adapted iteration *(left)*, and the reference mesh *(right)* of the two dimensional wedge.

A review article by Miller & Bailey [33] studies the experiments of the 18th and 19th centuries for different Mach numbers $0.2 \leq M \leq 2.0$ at $Re \approx 10^7$. The analyses in the mentioned article show that the experimental data obtained three centuries ago are in good agreement to the modern data.

Sphere measurements obtained by [33] and [34] show that regardless of the diameter size of the sphere, the drag coefficient increases rapidly in the transonic region and for $M \geq 1.6$ and $Re \geq 10^5$ it stays to be constant with further increases in Reynolds number. Experimental analyses in [34] and earlier in [35] show that the drag coefficient slowly decreases when the Mach number increases above $M \geq 2$ for the flow with $Re \gtrapprox 10^6$. We leave a complete discussion for different Mach numbers for future research, but in this paper we present results for only one Mach number, in order to see if the G2 solution gives a correct result according to the experiment.

We use Algorithm 1 for the supersonic flow around a sphere with diameter $d = 0.074$ at Mach number $M = 2$. For this Mach number the flow characterized by a detached three dimensional bow shock wave in front of the sphere and is in a mixed subsonic and supersonic flow behind the sonic line $M = 1$. Here the pressure drag at the stagnation point is high compared to the subsonic case. An attached shock wave develops in the rear of the sphere, which is also counted as a substantial source of the pressure drag. Therefore, the area for the pressure stagnation point and attached shock waves should be resolved by computation for the correct drag coefficient. We observe from the results that the adaptive G2 method tries to resolve these regions.

We present the results from the simulation in Table III. 10% of the largest cells are refined during the adaptive algorithm. We start with an initial coarse mesh, which has 9 720 vertices and 53 312 cells, which reaches 168 820 vertices and 918 605 cells after 9th adaptive iteration. The error bound of the drag coefficient $\sum_{n,K} \eta_n^K$ converge by the mesh refinement, as the drag coefficient approximately stays around the experimental data $C_{dp} \approx 1$. In Figure 13 the drag coefficients are plotted after each adaptive iterations.

We plot the solution of the adaptive algorithm in Figure 11 after eight refinements. The right

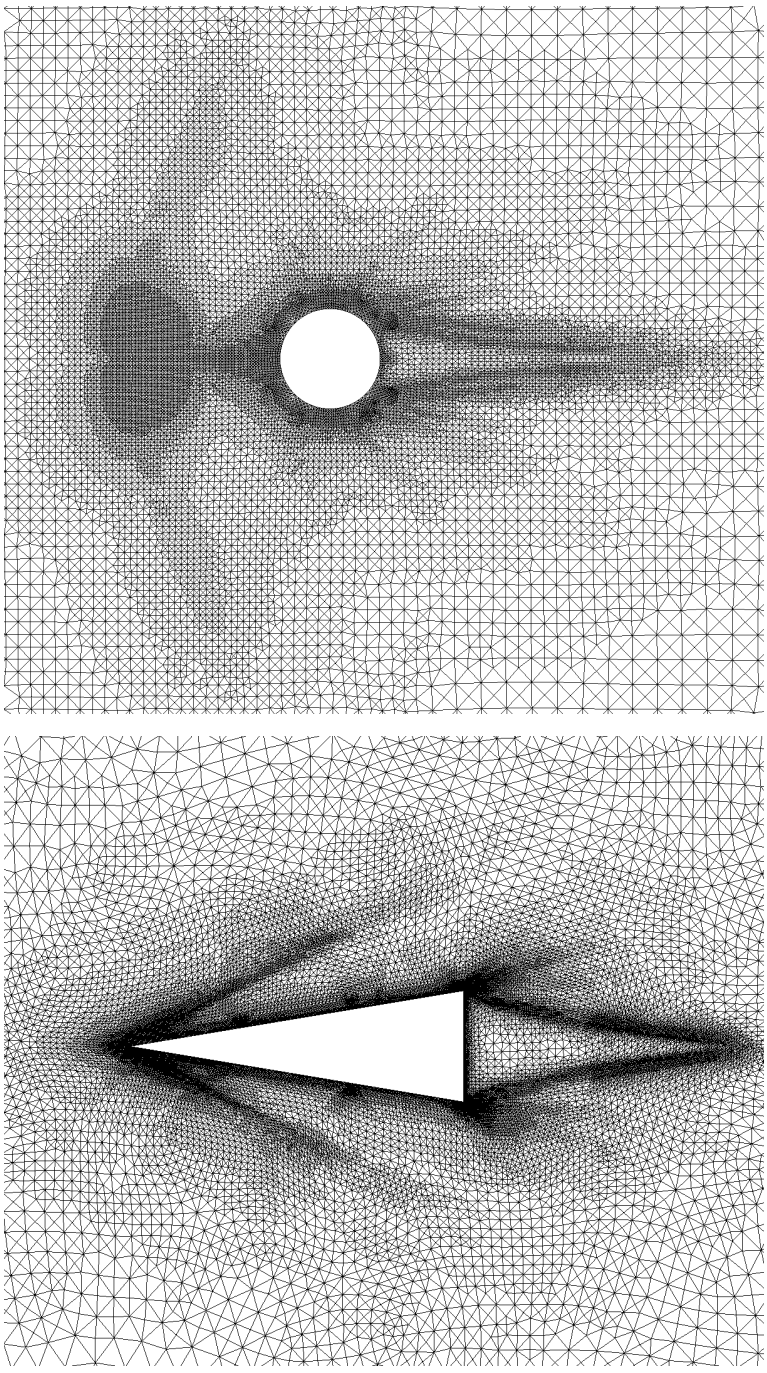

Figure 10. Adapted meshes for the 2D (*above*) cylinder after twelve, and wedge (*below*) after nine adaptive iterations.

column of the figure shows the primal solutions and the left column presents the corresponding dual solutions. The magnitude of the dual solution is high in the areas with the significant contribution to the pressure drag force. The plot of the primal pressure shows that already in eight adaptive step the pressure structures are close to be resolved.

In Figure 12 we present the initial coarse mesh and the mesh after nine adaptive refinements. After each refinement the boundary nodes, which appear from the Rivara algorithm are projected to the surface of the sphere. Also, we notice that similar to the 2D result, the algorithm focuses to resolve the pressure stagnation point, area of the sonic line and attached shock wave, which is expected since they are the main source of pressure drag. With ad hoc refinement, for instance residual based or gradient based adaptation, the region with strong shocks are well resolved. However, we notice that the duality based adaptive algorithm does not resolve a propagating bow shock and other strong discontinuities, it only refines the areas with the largest error contribution. Consequently, it significantly decreases the computational cost of the drag force computation.

Table III. The convergence history of the drag coefficient. Here $\bar{C}_{dp}$ is a mean value of C_{dp} over the time interval $[t-\epsilon_t, t]$, where ϵ_t is a small number, and $\sum_{n,K} \eta_n^K$ denotes a sum of error indicators.

#iter	#vertices	#cells	S	$\bar{C}_{dp}$	$\sum_{n,K} \eta_n^K$
0	9720	53312	0.8218	0.8115	1.5018
1	17405	94572	0.9571	0.8360	1.3096
2	22915	124884	1.1586	0.8502	1.0234
3	29686	160313	1.4233	0.9085	0.8651
4	39328	212637	1.6683	0.9474	0.7352
5	51746	280031	1.8440	0.9705	0.6236
6	69418	376144	2.0050	0.9873	0.5429
7	93696	508209	2.0538	0.9982	0.4532
8	126012	685079	2.1038	1.0046	0.3844
9	168820	918605	2.0541	1.0081	0.3199

9. Conclusion

We have presented an adaptive finite element method for the 3D time dependent compressible Euler equations, based on a posteriori error estimation of an output of interest, using sensitivity information from an associated dual problem based on the variables density, velocity and pressure, with the state law of a perfect gas. The a posteriori error estimation was based on a finite element method with continuous linear approximation in space and time, and streamline diffusion stabilization together with residual based shock-capturing, but the error estimation results are straight forward to extend to other finite element methods.

This paper can be seen as an extension of our previous work on adaptive finite element methods for turbulent incompressible flow [17, 16, 18, 19], to compressible flow. The basic tools of a posteriori error estimation are now extended to compressible flow, and future work

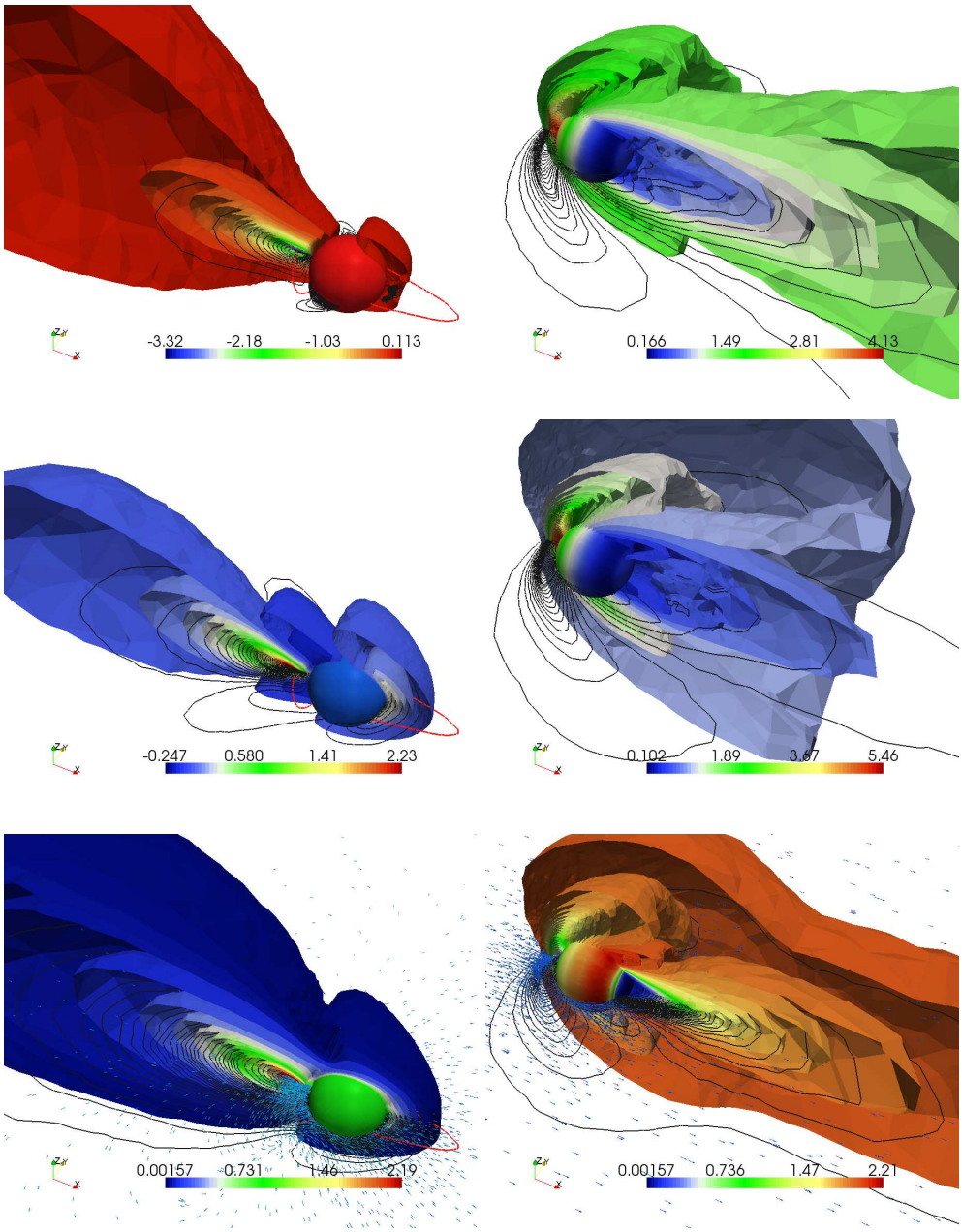

Figure 11. Supersonic flow around a sphere: the dual solution at time $t = 0$ of density *(top-left)*, pressure *(middle-left)* and magnitude of velocity *(bottom-left)*; the primal solution at time $t = 0.5$ of density *(top-right)*, pressure *(middle-right)* and magnitude of velocity *(bottom-right)*. The contours are plotted in the collormap. The sonic line in red is plotted together with the dual solution.

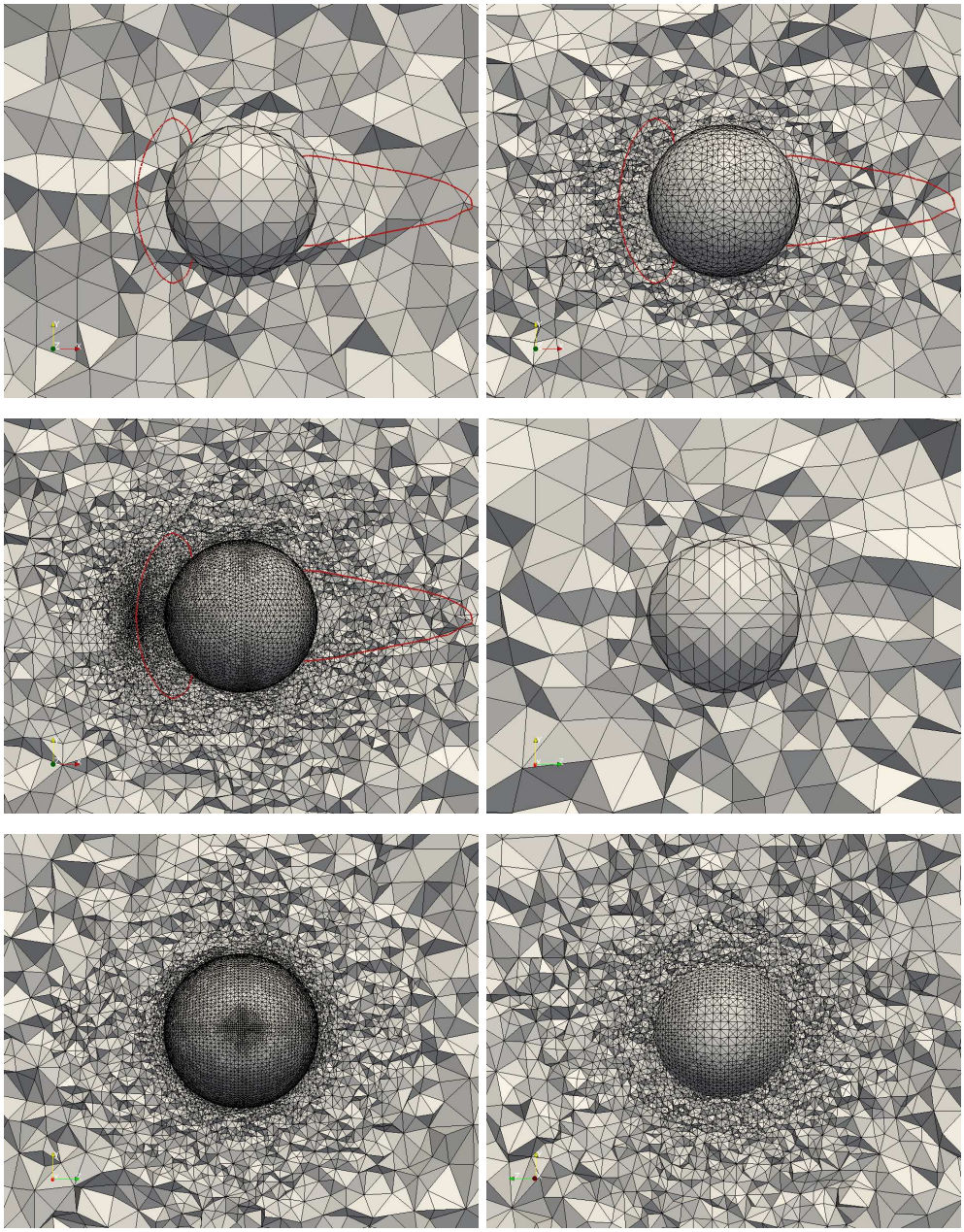

Figure 12. Supersonic flow around a sphere: the (x, y) - view of the mesh for the initial mesh *(top-left)*, four times *(top-right)* and nine times *(middle-left)* adaptive refinement according to the drag force together, the sonic line is plotted in red, (y, z) - view of the mesh for $x = x_s$ of the initial mesh *(middle-right)*, where x_s - is x coordinate of the center of sphere, the finest mesh close to the stagnation point of pressure $x = x_s - d/2$ *(below-left)*, and the finest mesh at $x = x_s + 0.02$ from back *(below-right)*

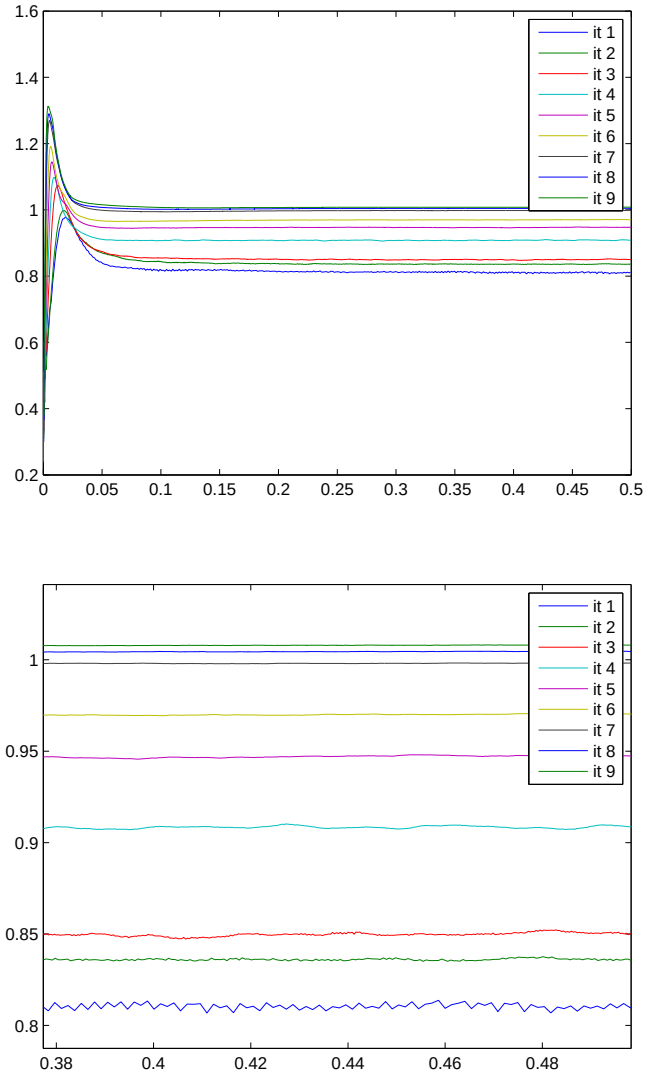

Figure 13. Supersonic flow around a sphere: the drag coefficient C_{dp} in different adaptive iterations.

will focus on studying the adaptive method for turbulence benchmarks problems, and to extend the method to viscous compressible flow modeled by the Navier-Stokes equations. Future work will also investigate the performance of different stabilized finite element methods, see e.g. [22], for applications to turbulent compressible flow.

10. Acknowledgements

This research is supported by the Swedish Research Council (VR) and the Swedish Foundation for Strategic Research (SSF).

REFERENCES

1. Löhner R. An adaptive finite element scheme for transient problems in CFD. *Computer Methods in Applied Mechanics and Engineering* 1987; **61**(3):323 – 338, doi:DOI: 10.1016/0045-7825(87)90098-3.
2. Mittal S, Aliabadi S, Tezduyar T. Parallel computation of unsteady compressible flows with the EDICT. *Comput. Mech.* 1999; **23**(2):151–157, doi:10.1007/s004660050395.
3. Eriksson K, Johnson C. An adaptive finite element method for linear elliptic problems. *Math. Comp.* 1988; **50**:361–383.
4. Eriksson K, Estep D, Hansbo P, Johnson C. Introduction to adaptive methods for differential equations. *Acta Numer.* 1995; **4**:105–158.
5. Eriksson K, Estep D, Hansbo P, Johnson C. *Computational Differential Equations*. Cambridge University Press New York, 1996.
6. Becker R, Rannacher R. A feed-back approach to error control in adaptive finite element methods: Basic analysis and examples. *East-West J. Numer. Math.* 1996; **4**:237–264.
7. Becker R, Rannacher R. A posteriori error estimation in finite element methods. *Acta Numer.* 2001; **10**:1–103.
8. Johnson C, Szepessy A. Adaptive finite element methods for conservation laws based on a posteriori error estimates. *Commun. Pure. Appl. Math* 1995; **48**:199–234.
9. Johnson C, Szepessy A, Hansbo P. On the convergence of shock-capturing streamline diffusion finite element methods for hyperbolic conservation laws. *Mathematics of Computation* 1990; **54(189)**:107–129.
10. Johnson C. *Adaptive Finite Element Methods for Conservation Laws*. Advanced Numerical Approximation of Nonlinear Hyperbolic Equations, Springer Lecture Notes in Mathematics, Springer Verlag, 1998; 269–323.
11. Hartmann R. Adaptive FE Methods for Conservation Equations. *Hyperbolic Problems: theory, numerics, applications: eighth international conference in Magdeburg, February, March 2000*, *International series of numerical mathematics*, vol. 141, Freistühler H, Warnecke G (eds.), Birkhäuser, Basel, 2001; 495–503.
12. Houston P, Hartmann R. Goal–oriented a posteriori error estimation for compressible fluid flows. *Numerical Mathematics and Advanced Applications*, Brezzi F, Buffa A, Corsaro S, Murli A (eds.), Springer, 2003; 775–784.
13. Houston P, Hartmann R, Süli A. Adaptive discontinuous Galerkin finite element methods for compressible fluid flows. *Numerical methods for Fluid Dynamics VII, ICFD*, Baines M (ed.), 2001; 347–353.
14. Larson M, Barth TJ. A posteriori error estimation for discontinuous Galerkin approximations of hyperbolic systems. *In Discontinuous Galerkin Methods, B. Cockburn, G. Karniadakis, and C.-W. Shu, editors, Lecture Notes in Comput. Sci. Engrg., 11, Springer, Berlin* 2000; :363–368.
15. Burman E. Adaptive finite element methods for compressible flow. *Computer methods in applied mechanics and engineering* 2000; **190**:1137–1162.
16. Hoffman J, Johnson C. A new approach to computational turbulence modeling. *Comput. Methods Appl. Mech. Engrg.* 2006; **195**:2865–2880.
17. Hoffman J. Computation of mean drag for bluff body problems using adaptive DNS/LES. *SIAM J. Sci. Comput.* 2005; **27(1)**:184–207.
18. Hoffman J. Adaptive simulation of the turbulent flow past a sphere. *J. Fluid Mech.* 2006; **568**:77–88.
19. Hoffman J. Efficient computation of mean drag for the subcritical flow past a circular cylinder using General Galerkin G2. *International Journal of Numerical Methods in Fluids* 2009; **59(11)**:1241–1258.
20. Tezduyar TE, Hughes TJR. Finite element formulations for convection dominated flows with particular

emphasis on the compressible Euler equations. *Proceedings of AIAA 21st Aerospace Sciences Meeting, AIAA Paper 83-0125, Reno, Nevada* 1983; .
21. Hughes TJR, Tezduyar TE. Finite element methods for first-order hyperbolic systems with particular emphasis on the compressible Euler equations. *Computer Methods in Applied Mechanics and Engineering* 1984; **45**(1-3):217 – 284, doi:DOI: 10.1016/0045-7825(84)90157-9.
22. Tezduyar TE, Senga M. Stabilization and shock-capturing parameters in SUPG formulation of compressible flows. *Computer Methods in Applied Mechanics and Engineering* 2006; **195**:1621–1632.
23. Johnson C, Szepessy A. *Shock-capturing streamline diffusion finite element methods for nonlinear conservation laws*. Recent Developments in Computatioonal Fluid Dynamics, edited by T. J. R. Hughes and T.E. Tezduyar, AMD-Vol 95, 1988.
24. Le Beau GJ, Ray SE, Aliabadi SK, Tezduyar TE. SUPG finite element computation of compressible flows with the entropy and conservation variables formulations. *Computer Methods in Applied Mechanics and Engineering* 1993; **104**(3):397 – 422, doi:DOI: 10.1016/0045-7825(93)90033-T.
25. Martineau RC, Berry R. Characteristic boundary conditions for the two-step Taylor-Galerkin FEM. *Computer Methods in Applied Mechanics and Engineering* 2006; **195**(7-8):742 – 762, doi:DOI: 10.1016/j.cma.2005.02.017.
26. Evans LC. *Partial Differential Equations*. American Mathematical Society, 1998.
27. Catabriga L, Coutinho ALGA, Tezduyar TE. Compressible flow SUPG parameters computed from element matrices. *Communications in Numerical Methods in Engineering* 2005; **21**:465–476.
28. Catabriga L, Coutinho ALGA, Tezduyar TE. Compressible flow SUPG parameters computed from degree-of-freedom submatrices. *Computational Mechanics* 2006; **38**:334–343.
29. Catabriga L, de Souza DAF, Coutinho ALGA, Tezduyar TE. Three-dimensional edge-based SUPG computation of inviscid compressible flows with YZβ shock-capturing. *Journal of Applied Mechanics* 2009; **76**(2):021208.
30. Tezduyar TE, Senga M, Vicker D. Computation of inviscid supersonic flows around cylinders and spheres with the SUPG formulation and YZβ shock-capturing. *Computational Mechanics* 2006; **38**:469–481.
31. Rispoli F, Saavedra R, Menichini F, Tezduyar TE. Computation of inviscid supersonic flows around cylinders and spheres with the V-SGS stabilization and YZβ shock-capturing. *Journal of Applied Mechanics* 2009; **76**(2):021209.
32. Rivara MC. Local modification of meshes for adaptive and/or multigrid finite-element methods. *Journal of Computational and Applied Mathematics* 1992; **36**(1):78–89.
33. Miller DG, Bailey AB. Sphere drag at mach numbers from $0 \cdot 3$ to 20 at reynolds numbers approaching 10^7. *Journal of Fluid Mechanics Digital Archive* 1979; **93**(03):449–464.
34. Bailey A, Hiatt J. Free-flight measurements of sphere drag at subsonic, transonic, supersonic, and hypersonic speeds for continuum, transition, and near free molecular flow conditions. *Arnold Engng Development Ctr., Arnold Air Force Station, TN, Rep. AEDC-TR-70-291* 1971; .
35. Charters A, Thomas R. The aerodynamic performance of small spheres from subsonic to high supersonic velocities. *Journal of the Aeronautical sciences* 1945; **12**:468–476.